



Article

Holocene Paleoclimate Records in Equatorial West Africa: Insights Based on the Characterization of Glycerol Dialkyl Glycerol Tetraethers

Peining Yang ^{1,2} , Shengyi Mao ¹, Yiyun Cao ^{1,3}, Li Liu ^{1,3}, Mengyue Zhai ⁴, Zhongyan Qiu ⁵  and Lihua Liu ^{1,*}

¹ Guangzhou Institute of Energy Conversion, Chinese Academy of Sciences, Guangzhou 510640, China; peining518@mail.ustc.edu.cn (P.Y.); maosy@ms.giec.ac.cn (S.M.); caoyy@ms.giec.ac.cn (Y.C.); lliu0623@mail.ustc.edu.cn (L.L.)

² University of Chinese Academy of Sciences, Beijing 100049, China

³ Department of Thermal Science and Energy Engineering, School of Engineering Science, University of Science and Technology of China, Hefei 230026, China

⁴ Department of Marine Science, School of Ocean Sciences, China University of Geosciences, Beijing 100083, China; zhaimy1206772419@163.com

⁵ Key Laboratory of Submarine Geosciences, Second Institute of Oceanography, Ministry of National Resources, Hangzhou 310012, China; qiuzy@sio.org.cn

* Correspondence: liulh@ms.giec.ac.cn; Tel.: +86-020-3722-3742

Abstract: One gravity core retrieved from the Niger Delta was used to explore the origin of deposited organic matter (OM) and the paleo-climatic and environmental conditions over the Holocene in equatorial West Africa. The geochemical properties of sediments including glycerol dialkyl glycerol tetraethers (GDGTs) and elemental (%OC, %N, C/N) and isotopic ($\delta^{13}\text{C}_{\text{org}}$, $\delta^{15}\text{N}$) signatures were determined. The determination constrained the age of the column and revealed that the sediment OM was mainly derived from a marine source. The isoprenoid (iso)GDGTs were the dominant GDGTs, with a small amount of branched (br)GDGTs, which led to a low-branched and isoprenoid tetraether index (BIT, 0.02–0.21) and represented a low terrestrial input. Most isoGDGTs and OH-GDGTs were produced in situ by Marine Group I (MG-I) *Thaumarchaeota*, while the brGDGTs were mainly transported from land. A two-endmember model quantified the contribution of terrestrial OM, as 0.9–19.9% by BIT and 1.1–32.6% by $\delta^{13}\text{C}$. Accordingly, the millennium-scale sea surface temperatures (SSTs) were reconstructed based on the cyclopentane ring distribution ($\text{TEX}_{86}^{\text{H}}$) and the ring index of OH-GDGTs (RI-OH). The top core SSTs were lower than the modern mean annual SST due to the growth season and habitat depth of *Thaumarchaeota*. The reconstructed SSTs clearly revealed the four stages of paleoclimate change, in particular, the drought episode of 8.2 kyr and the following humid period. The above research has enhanced our understanding of the paleoclimate change in river outflow during the Holocene at the millennium scale.

Keywords: Gulf of Guinea; *Thaumarchaeota*; glycerol dialkyl glycerol tetraethers; sea surface temperatures; OM source



Citation: Yang, P.; Mao, S.; Cao, Y.; Liu, L.; Zhai, M.; Qiu, Z.; Liu, L. Holocene Paleoclimate Records in Equatorial West Africa: Insights Based on the Characterization of Glycerol Dialkyl Glycerol Tetraethers. *Water* **2024**, *16*, 771. <https://doi.org/10.3390/w16050771>

Received: 31 January 2024

Revised: 23 February 2024

Accepted: 28 February 2024

Published: 5 March 2024



Copyright: © 2024 by the authors. Licensee MDPI, Basel, Switzerland. This article is an open access article distributed under the terms and conditions of the Creative Commons Attribution (CC BY) license (<https://creativecommons.org/licenses/by/4.0/>).

1. Introduction

Deltas and deep-sea fans represent the active interface of land and ocean and possess more than 50% of global organic carbon [1]. Their sediments are optimal to investigate the pathway and fate of buried organic matter (OM) and are a valuable archive in the understanding of global carbon cycling and the reconstruction of the paleoclimate and its environment [2].

Among these areas, the Niger Delta is one of the largest deltaic systems and a major hydrocarbon-rich province, in which the river stream deposits sediments, containing various amounts of OM from West Africa through the Niger River [3]. Previous research has mainly focused on oil exploration and exploitation or on thermal maturity [4].

Some researchers have investigated the paleoenvironmental change in the adjacent Congo Province [5]. Only a few studies have assessed the sources, transportation, and fate of OM in the sediment [1]. The key to understanding the paleoclimate and its environment is the reconstruction of the paleo sea surface temperature (SST). The reconstruction of the SST has mostly referred to the intra-seasonal SST with satellite data, with little reconstruction of the sediments at the millennium scale [6]. The understanding of OM sources and paleo SST corresponding to the paleoclimate change in the area is still limited.

The source of OM can be traced by the bulk organic parameters, TOC, TN, the ratio of organic carbon to total nitrogen (C/N), and the isotope signatures of $\delta^{13}\text{C}$ and $\delta^{15}\text{N}$ [7]. The typical SST proxies include Mg/Ca and $\delta^{18}\text{O}$ of foraminifera [8], the U_{37}^{K} index based on long-chain ketones [9], and the long-chain diol index (LDI) [10].

Recently, organic biomarker proxies have been increasingly used to trace the source of sedimentary OM and to reconstruct the paleoclimatic conditions. The multiple sources may result in the overlap of C/N and stable isotope signatures of OM [11]. The error and overlap could be discerned by the composition of glycerol dialkyl glycerol tetraethers (GDGTs) and the derived indicators [12]. GDGTs, the reliable proxies of the paleoenvironment and paleoclimate, attract more research attention since they are preserved over geological time [13] and reveal the OM source [14], sea water temperature [15], and the structure of the microbial community [13].

GDGTs are usually divided into isoprenoid (isoGDGTs) and branched (brGDGTs). IsoGDGTs are derived generally from phylum *Thaumarchaeota* (ammonia-oxidizing archaea) and commonly exist in marine environments [16]. BrGDGTs, produced by anaerobic bacteria, are abundant in soil, peat, and lake and river sediment [13]. OH-GDGTs, newly determined isoGDGTs, are categorized further into OH-0, OH-1, and OH-2 and have been also found in methanogenic *Euryarchaeote* *M. thermolithotrophicus* [17] and Group 1.1a *Thaumarchaeotes* [13].

The branched and isoprenoid tetraether (BIT) index [14] represents the proportion of brGDGTs to *Crenarchaeol* and can assess the input of terrestrial OM in a marine setting [18]. The cyclopentane ring distribution of GDGTs in the surface sediment correlates with the SST, which has led to a novel proxy, TEX_{86} (Equation (1) in Table 1b) [19], being used to reconstruct the SST (Equations (2) and (3) in Table 1b) [20]. Modified TEX_{86} , $\text{TEX}_{86}^{\text{H}}$ and $\text{TEX}_{86}^{\text{L}}$, was later proposed to determine an environment with an annual SST of $>15\text{ }^{\circ}\text{C}$ and $<15\text{ }^{\circ}\text{C}$, respectively [21]. Furthermore, the ring index of OH-GDGTs (RI-OH) is suitable for the convenient reconstruction of the tropical warm SST, especially for the tropical estuarine and coastal areas [22]. An error may be present in the estimation of the SST in which GDGTs are derived from both terrestrial archaea and marine methanogens [23]. Fortunately, the GDGTs-related indexes can modify this kind of error.

Here, GDGT-based proxies and other organic determinations were used to investigate the source of OM and reconstruct the SST in the mouth of the Niger Delta basin. This investigation provides novel paleoenvironmental data for the African Humid Period (AHP) and a better understanding of the OM source and hydrological condition at the millennium scale.

2. Geological and Climate Background

The Niger Delta is located in the east of the equatorial Atlantic [24] and is bound in the south by the Gulf of Guinea (GOG) [4]. The delta originated from the rifting of the Gondwana during the Late Jurassic to Neocomian [25] and the two large folds and thrust belts in the deep waters of the delta. The delta is composed of three main lithostratigraphic units, the Akata, Agbada, and Benin Formations, and the study area is located between the first two units [25].

The Niger Delta lies within the wet equatorial climatic region and is influenced mainly by the convection of the West African monsoon (WAM) [3], which regulates the moisture and heat budget of the atmosphere of low latitude and is closely related to the SST of eastern equatorial Atlantic (EEA) [24]. It is a typical monsoon region with two distinct

seasons, the summer rainy season and the winter dry season [3]. The intensity and the extent of the southwest monsoon, and the main wind system in east of the GOG is related to the seasonal migration of the tropical convergence zone (ITCZ) [26]. When the ITCZ approaches the equator in boreal winter, the surface temperature is the highest and vice versa (Figure 1 Left). The surface and subsurface ocean circulation there is controlled by the Guinea Current [6]. In boreal summer–fall, the current is strong and brings cool and salty surface water [27], and the reverse is true in boreal winter. The Niger River drains a large part of West Africa and discharges sediment-laden water into the Atlantic Ocean [28].

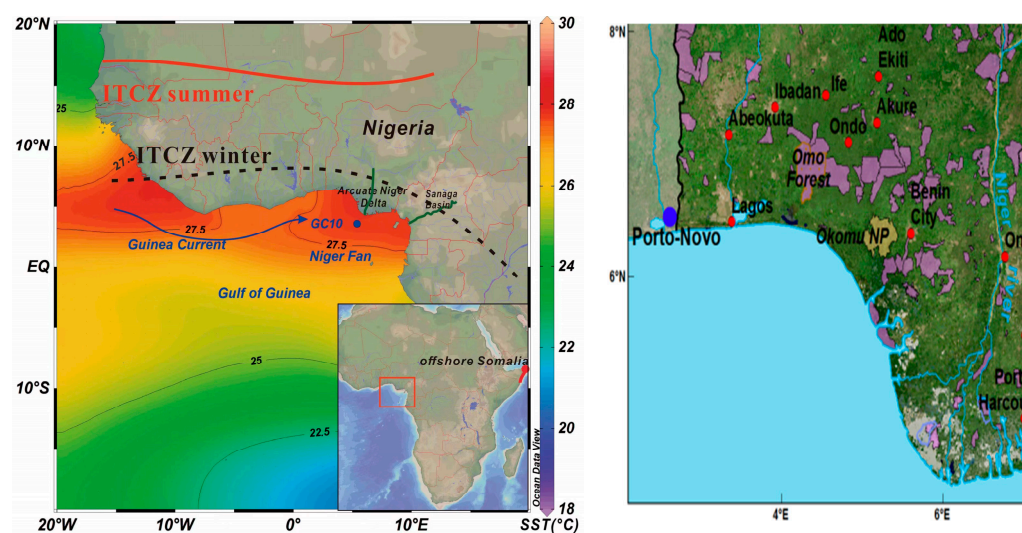


Figure 1. Geological background of the Niger Delta. **(Left):** Locations of the discussed record and modern SST in the Gulf of Guinea; blue arrows indicate the Guinea Current (GC). The surface location of the Intertropical Convergence Zone (ICTZ) in northern winter (black dotted line) and northern summer (solid red line). Two green lines represent the main rivers that converge into the Gulf of Guinea (Niger River and Sanaga River). Plot modified from Ocean Data view. **(Right):** Niger River System and major cities; the blue dot represents the capital (modified from The Republic of Nigeria, West Africa).

3. Materials and Methods

3.1. Sampling

One gravity core (GC)10 ($3^{\circ}34'15.08''$ N, $5^{\circ}24'19.39''$ E) was retrieved on the north-east of the Niger Delta in February 2020 (Figure 1) during the 57IV cruise, in which the water depth was 1418 m. The core was 199 cm length and sectioned at 2 cm; in total, 67 sub-samples were collected and stored at -20°C until further analysis.

3.2. AMS ^{14}C Dating

Globigerinoides ruber (*G. ruber*) and *Globigerinoides sacculifer* (*G. sacculifer*) were chosen from seven samples and sent to Beta Analytic Inc., Miami, FL, USA, for Accelerator Mass Spectrometry (AMS) ^{14}C dating. Five samples contained more than 6 mg of *G. ruber* and *G. sacculifer* foraminifera shells, and the standard AMS dating was used, while the two others (depth of 142 and 199 cm) with less than 4 mg adopted Micro-sample (MS) AMS dating. The raw ^{14}C data were calibrated using the Marine 20 dataset [29] and expressed in calibrated years BP (years before 1950).

3.3. TOC, TN, and Stable Isotopes Analysis

The sediment was freeze-dried and ground into powder with an agate pestle. The samples were pre-treated with 6 N HCl for 24 h to remove carbonate and rinsed with deionized water to remove salt. The TOC and TN were determined using a Thermo Fisher

Scientific FLASH EA 1200 Series CNS at Guangdong Ocean University, with a 1σ precision of ± 0.02 wt %C and ± 0.003 wt %N. The TOC/TN (C/N) was also obtained.

The $\delta^{13}\text{C}$ and $\delta^{15}\text{N}$ were determined by a Finnigan DELTA ^{plus} XL mass spectrometer, and the determination was expressed in δ as the deviation from the standard reference material in parts per mil (‰). The reference was Vienna PeeDee Belemnite (VPDB) for $\delta^{13}\text{C}$ and atmospheric nitrogen for $\delta^{15}\text{N}$. The analytical precision was $\pm 0.2\text{‰}$ for $\delta^{13}\text{C}$ and $\pm 0.3\text{‰}$ for $\delta^{15}\text{N}$.

3.4. Glycerol Dialkyl Glycerol Tetraethers

The total lipid extract (TLE) of the sediment was obtained by Soxhlet extraction with DCM: MeOH (9:1 *v/v*) (Thermo Fisher Scientific Co., Ltd, Shanghai, China) at $47.5\text{ }^{\circ}\text{C}$ for 72 h. The solution was filtered and transferred to a 4 mL vial. To remove the particulate matter, the TLE was redissolved in a DCM filter through a $0.45\text{ }\mu\text{m}$ PTFE filter with 500 μL 99:1 (*v/v*) hexane: isopropanol (ANPEL laboratory Technologies Inc., Shanghai, China).

The GDGTs were analyzed by high-performance liquid chromatography/atmospheric pressure chemical ionization–mass spectrometry (HPLC/APCI-MS) at the Guangzhou Institute of Geochemistry, Chinese Academy of Sciences. The injection was 10 μL and separated by a Prevail Cyano 3 μm column (2.1 mm 150 mm Alltech, Deerfield, IL, USA) at $30\text{ }^{\circ}\text{C}$. The flow rate was 0.2 mL/min. The GDGTs were isocratically eluted with 99% hexane and 1% isopropanol for 5 min, followed by a linear gradient to 1.8% isopropanol within 50 min. Detection was conducted using atmospheric pressure positive ion chemical ionization MS (APCI-MS) via selected ion monitoring (SIM) of $[\text{M} + \text{H}]$ ions. The conditions were as follows: nebulizer pressure 60 psi, N_2 drying gas flow 6.0 L/min, gas temperature $200\text{ }^{\circ}\text{C}$, vaporizer temperature $400\text{ }^{\circ}\text{C}$, capillary voltage 2500 V, corona current 5 μA .

3.5. GDGTs Proxies and SST Estimation

The GDGT-based indices and the SST reconstruction are listed in Table 1.

Table 1. GDGT proxies and SST estimation.

(a) GDGT Proxies	References
(1) $\text{BIT} = \frac{([\text{GDGT-Ia}] + [\text{GDGT-IIa}] + [\text{GDGT-IIIa}])}{([\text{GDGT-Ia}] + [\text{GDGT-IIa}] + [\text{GDGT-IIIa}] + [\text{Cren}])}$	[14]
(2) $\text{MI} = \frac{[\text{GDGT-1}] + [\text{GDGT-2}] + [\text{GDGT-3}]}{([\text{GDGT-1}] + [\text{GDGT-2}] + [\text{GDGT-3}] + [\text{Cren}])}$	[30]
(3) $\% \text{GDGT-2} = \frac{\text{GDGT-2}}{[\text{GDGT-1}] + [\text{GDGT-2}] + [\text{GDGT-3}] + [\text{Cren}]}$	[31]
(4) $\text{DC} = \frac{[\text{GDGT-Ib}] + [\text{GDGT-IIb}]}{([\text{GDGT-Ia}] + [\text{GDGT-IIa}] + [\text{GDGT-Ib}] + [\text{GDGT-IIb}])}$	[32]
(b) SST Indices and Estimation	References
(1) $\text{TEX}_{86} = \frac{([\text{GDGT-2}] + [\text{GDGT-3}] + [\text{Cren}])}{([\text{GDGT-1}] + [\text{GDGT-2}] + [\text{GDGT-3}] + [\text{Cren}])}$	[19]
(2) $\text{TEX}_{86}^{\text{H}} = \log(\text{TEX}_{86})$	[21]
(3) $\text{SST} = 68.4 \times (\text{TEX}_{86}^{\text{H}}) + 38.6$	[21]
(4) $\text{RI} - \text{OH} = \frac{[\text{OH-GDGT-1}] + 2 \times [\text{OH-GDGT-2}]}{[\text{OH-GDGT-1}] + [\text{OH-GDGT-2}]}$	[22]
(5) $\text{SST} = 35.71 \times \text{RI} - \text{OH} - 32.86$	[22]
(6) $\text{SST}_{\text{summer}} = (\text{RI} - \text{OH} - 0.005) / 0.057$	[22]
(7) $\text{SST} = -(\text{OH-2} / \text{OHs} - 2.74) / 0.087$	[33]

4. Results

4.1. Age Model

The AMS ^{14}C data of the core are shown in Table 2. The time scale (>8 kyr BP) covered the significant climate perturbations during the early Holocene and the more humid conditions in Africa. The sedimentation rate was high in the early–mid Holocene (~ 7 kyr BP, average of ~ 55.2 cm/kyr), and it decreased to 23.3 cm/kyr during the whole

AHP, while it fell to ~ 18.8 cm/kyr after the AHP; the peak was ~ 8.4 kyr BP and sharply declined after 8.2 kyr BP (Figure 2a,b).

Table 2. Details of the foraminifera AMS ^{14}C dating of the GC10 core.

Depth (cm)	^{14}C Age (yr BP)	Calibrated Age (yr BP)
13	1080 ± 30	914 ± 146
37	1860 ± 30	1733 ± 157
67	3720 ± 30	4056 ± 175
109	5230 ± 30	5857 ± 168
142	6520 ± 30	7276 ± 140
182	7510 ± 30	8225 ± 145
199	7740 ± 30	8474 ± 137

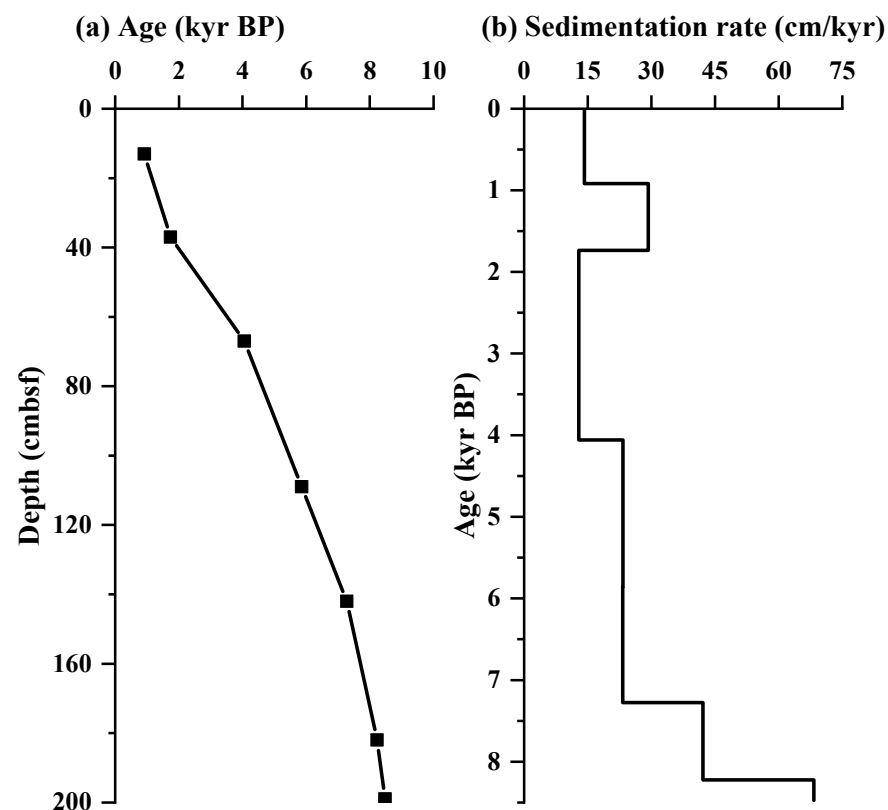


Figure 2. (a) Age–depth model and (b) sedimentation rate of core GC10 in the Niger fan.

4.2. Four Stages Indicated by $\delta^{13}\text{C}$, $\delta^{15}\text{N}$, and TOC/TN

The TOC decreased with depth from 1.23% to 1.87% (Figure 3). The TN had a similar profile to the TOC; it changed from 0.13 to 0.19%, with an average of 0.15%. The C/N ratio changed from 10.5 to 13. The $\delta^{13}\text{C}$ varied between -22.3 and -20.1 ‰, and the $\delta^{15}\text{N}$ was opposite to the $\delta^{13}\text{C}$, from 4.1 to 5.0‰.

Four stages can be defined based on the variations in the OM. The TOC, TN, and C/N ratio were lowest in the period of ca. 8.5–8 kyr BP. Then, all of these indicators increased gradually to the peak, whereas $\delta^{13}\text{C}$ and $\delta^{15}\text{N}$ showed bilateral symmetry from 8 to 5.5 kyr BP, and the 5.5–4.7 kyr BP showed a decrease in the TOC, C/N, $\delta^{15}\text{N}$, and stable TN and an increase in the $\delta^{13}\text{C}$. After 4.7 kyr BP, the TOC and TN rose gradually, and the $\delta^{13}\text{C}$ and $\delta^{15}\text{N}$ showed the opposite tendency.

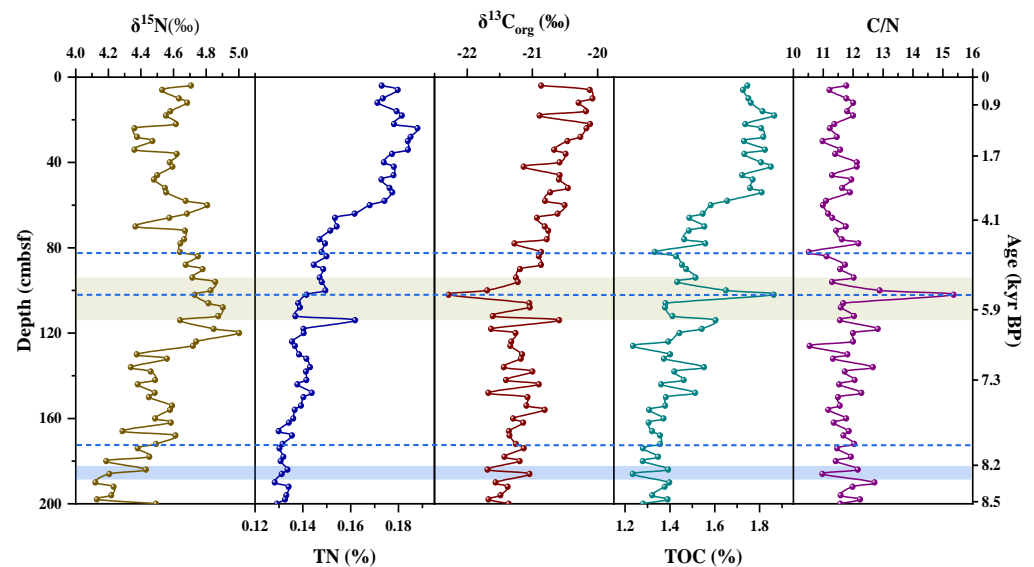


Figure 3. The profile of $\delta^{15}\text{N}$, TN (total nitrogen), $\delta^{13}\text{C}$, TOC (total organic carbon), and C/N (TOC/TN). The blue bar marks the 8.2 kyr BP, and the brown bar marks the end of the humid period. The blue dashed line divides the five main stages of bulk organic parameters.

4.3. Distribution of GDGTs

All isoGDGTs, brGDGTs, and OH-GDGTs were detected in the sediment samples (Figure 4). The isoGDGTs comprised 93%, higher than the brGDGTs and OH-GDGTs. The brGDGTs contributed 6.9% to the total GDGTs, while the OH-GDGTs were less than 0.8% (Figure 4c). *Crenarchaeol* (*Cren*) and GDGT-0 were the dominant isoGDGTs in all samples, accounting for 34.3–51.3% and 19.3–35.9%, respectively. Only small amounts of GDGT-1, -2, and -3 and the *Cren* isomer (*Cren'*) were detected (Figure 4a). The isoGDGTs decreased downcore, while the brGDGTs generally increased.

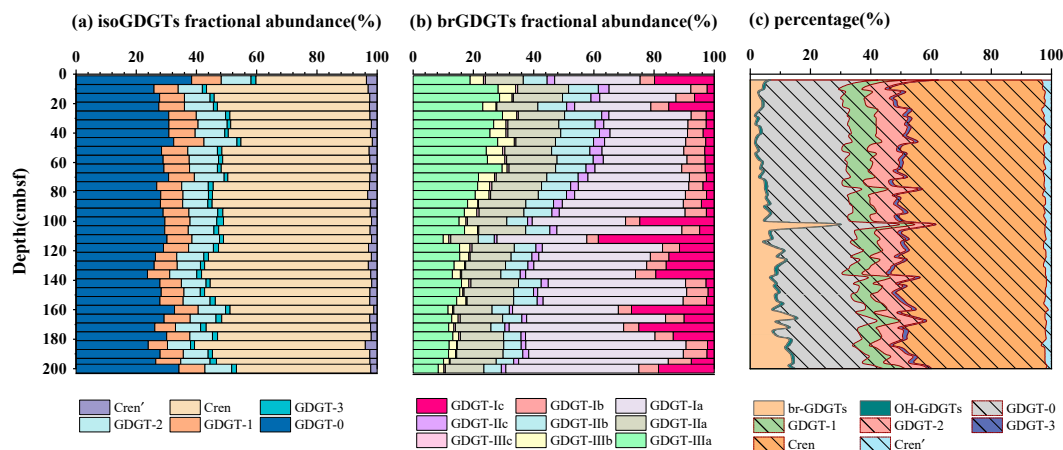


Figure 4. The contribution of (a) specific isoGDGTs (isoprenoid glycerol dialkyl glycerol tetraethers) and (b) brGDGTs (branched glycerol dialkyl glycerol tetraethers) and (c) the profiles of each type of GDGT in core GC10.

4.4. SST Reconstruction Based on TEX^H_{86} and RI-OH Indexes

The SST (Figure 5) in the Niger Delta was reconstructed by the TEX^H_{86} (Equations (2) and (3) in Table 1b) and the RI-OH; it was 20.7 to 26.7 °C and 20.7 to 25 °C (Equations (4) and (5) in Table 1b), respectively. The SSTs dropped at 8.4–8.2 kyr BP and slightly reduced during the humid period; then, they increased.

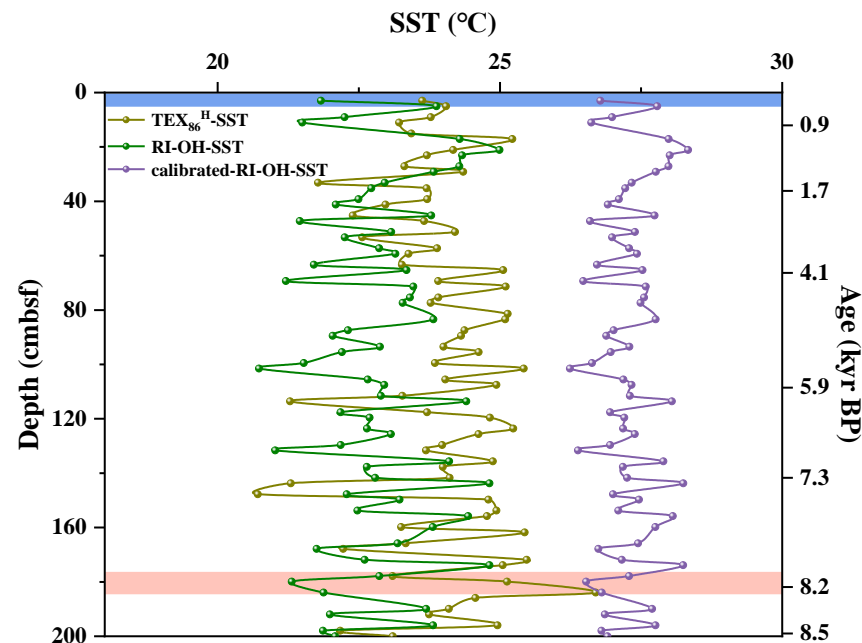


Figure 5. SST (sea surface temperatures) reconstructed by various indices. The blue area indicates the surface temperature, and the brown bar marks the SST trends of the ~8.2 kyr BP.

5. Discussion

5.1. Variation in the Sources of OM during the Holocene

The proxies determined here (-22.28 to -20.08‰ for $\delta^{13}\text{C}$, 4.12 to 5‰ for $\delta^{15}\text{N}$, and 10.5 to 13 for C/N) suggested a mixture of sources of the sediment in the Niger fan. The typical $\delta^{13}\text{C}$ of land C_3 plants is -21 to -32‰ [34], that of C_4 plants is -16 to -10‰ , and that of marine phytoplankton is -18 to -21‰ [35]. Terrestrial plants have a $\delta^{15}\text{N}$ -5 to 18‰ [36], while the marine OM is 4 – 9‰ [34]. The marine C/N ratio is 5 – 8 and >15 for land OM [35]. However, the $\delta^{15}\text{N}$ may be inadequate for source estimation due to the additional fractionation of nitrogen fixation and the denitrification and degradation of OM [37]. The positive correlation of the TOC and TN (Supplementary Figure S1c) indicated that most nitrogen was organic [38]. The BIT index (0.02 to 0.21 , average 0.06 , Equation (1) in Table 1a) revealed a lower contribution of land OM to the aquatic environment, since the BIT generally ranges 0.0 – 0.1 in a marine environment and 0.8 – 1.0 in land soil [39].

To further evaluate the contribution of the land OM in the delta, the two-endmember mixing model, $f_{\text{terr}} = (X_{\text{mar}} - X_{\text{sample}})/(X_{\text{mar}} - X_{\text{terr}})$, was applied [40], where f_{terr} is the fraction of terrestrial OM, X_{sample} can be the BIT or $\delta^{13}\text{C}$ of the sample, and X_{mar} and X_{terr} are the marine and land endmembers of the BIT or $\delta^{13}\text{C}$, respectively. The calculated contribution was 0.9 – 19.9% (Figure 6b), adopting the equatorial Atlantic (0.03) and the African soil (0.92) for the BIT [41]. For $\delta^{13}\text{C}$, the marine endmember of $\delta^{13}\text{C}$ is -20‰ , and the land endmember is -27‰ , which use the value of C_3 plants [35], which is the dominant land material in the equatorial Atlantic Ocean [42]. The estimated land OM from the $\delta^{13}\text{C}$ was 1.1% to 32.6% , broader than that estimated using the BIT (Figure 6b). Both estimations (Figure 6) were consistent with the determination of riverine Ba/Ca after ~ 5100 kyr BP [43], indicating a reduction in the land input during the late Holocene. The narrower fraction calculated by the BIT may be due to the fact that the BIT represents only the soil OM rather than the plant OM [13]. This further suggested that soil OM was the main land OM delivered to the sediments (Figure 6).

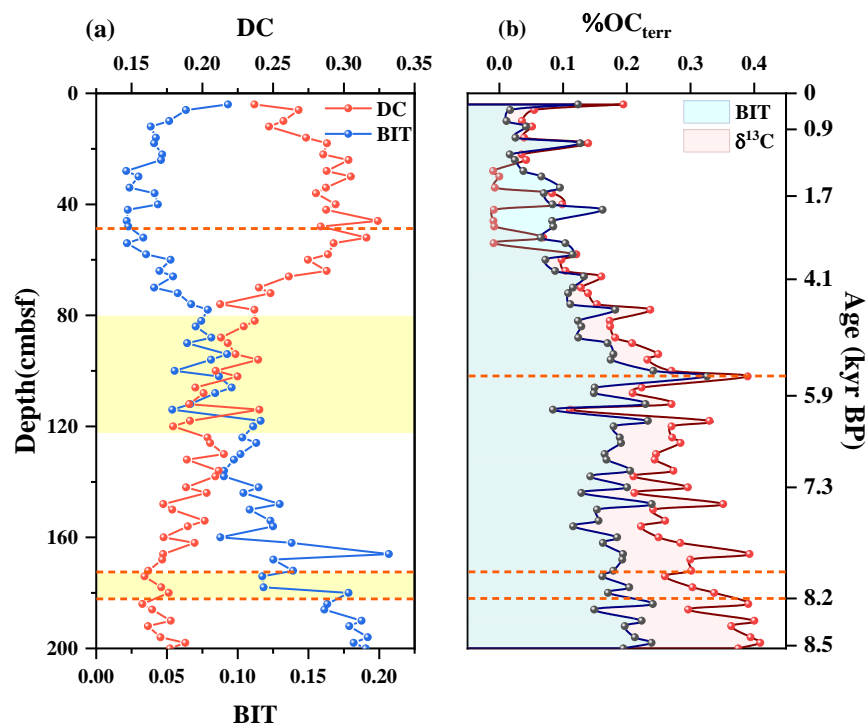


Figure 6. (a) Profile of BIT (branched and isoprenoid tetraether index) and DC (degree of cyclization of brGDGTs) of the core GC10. (b) Percentage of soil organic carbon (%OC_{terr}) or terrestrial organic carbon (%OC_{soil}) based on a binary mixing model of $\delta^{13}\text{C}$ and BIT.

During the early–mid Holocene, the TOC, TN, C/N, and BIT index were at their lowest, and the sedimentation rate rapidly declined, indicating a lower land OM input. This was caused by the reduction in the rainfall and thus in the river discharge that was ebbed away (Figures 3 and 6), as an interruption of the 8.2 kyr BP event and an abrupt and widespread instability of a dry and cool period in the Holocene [44]. This was likely initiated by a catastrophic outflow of the proglacial Lakes Agassiz and Ojibway, with the subsequent disruption in the Atlantic meridional overturning circulation [45]. The dry event during 8.5–7.8 kyr BP was also revealed by the low lake levels in Africa (i.e., Bosumtwi, Challa, Tana) [46].

Around 5.5 kyr BP, the TOC, TN, and C/N increased to the peak, rapidly recovering to warm–wet during the AHP. The increase in the TOC and BIT suggested the deposition of land OM, and the decrease in the $\delta^{13}\text{C}$ and the increase in the C/N reflected the high flow of fresh water.

Prevailing in ca. 5.5–4.7 kyr BP, the lower input of land OM caused a subsequent decrease in the TOC and C/N (Figure 3) under post-AHP drying conditions. This time-transgressive termination of the humid period revealed the decline in the rainfall intensity, which was induced directly by the decrease in the summer insolation and the gradual southward migration of the monsoon rain belt [5]. It was also consistent with the termination of the AHP at lower latitudes [5].

The TOC increased, and the BIT decreased during 4.7–3 kyr BP. After ~3 kyr BP, the TOC was high and varied smoothly, and the BIT increased gradually, representing a humid environment [47].

5.2. Sources of GDGTs during the Holocene

Abundant isoGDGTs with low brGDGTs and OH-GDGTs were determined here (Figure 4). The bulk GDGTs and their major components (isoGDGTs) were mainly derived from marine *Thaumarchaeotal* as indicated by the BIT, GDGT-0/*Cren*, GDGT-2/*Cren*, methane index (MI) (Equation (2) in Table 1a), and %GDGT-2 (Equation (3) in Table 1a).

The isoGDGTs, categorized further into GDGT-0, GDGT-1, GDGT-2, GDGT-3, *Cren*, and its regioisomer (*Cren'*) [19], originated mainly from Marine Group I (MG-I) *Thaumarchaeota* [16]. GDGT-0, -1, -2, and -3 could also be produced by Marine group II (MG-II) *Euryarchaeota* in shallow water [13]. GDGT-0 and *Cren* are typical biomarkers for *Thaumarchaeota* [31] and were dominant in the samples. The GDGT-0/*Cren* indicated the source of GDGTs (0–2 from *Thaumarchaeota*, and >2 from methanogenic archaea) [48]; the determined ratio (0.42 to 1.05) suggested that *Thaumarchaeota* was the principal source (Figure 7).

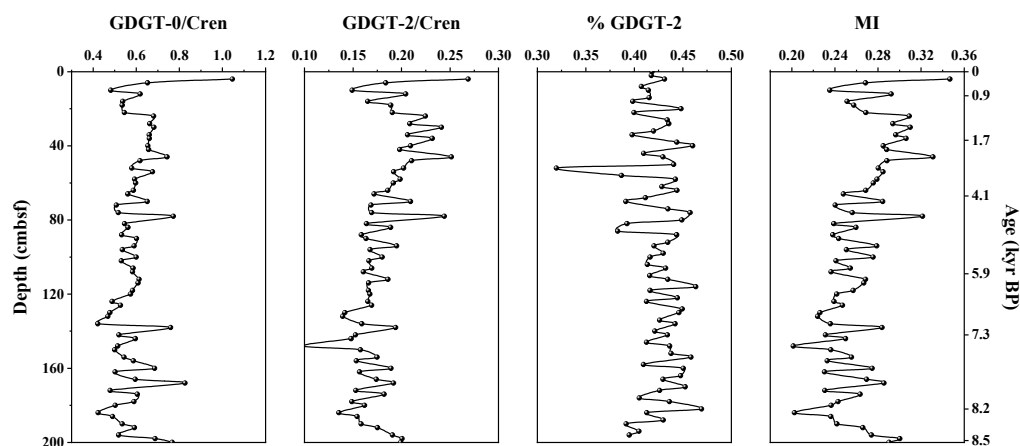


Figure 7. Distribution of GDGT-0/*Cren*, GDGT-2/*Cren* (GDGT-0–2, GDGTs with 0–2 cyclopentane rings; *Cren*, *Crenarchaeol*), %GDGT-2, and MI (Methane index).

The methane index (MI) can evaluate the contribution of GDGTs (GDGT-1, -2, and -3) derived from the methanotrophic archaea of MG-II *Euryarchaeota* [30]. The low determination of MI (average 0.26, <0.3), lower average %GDGT-2 (32 to 47, average <45) [15], and rare GDGT-2/*Cren* (0.10–0.27, <0.4) [49] indicated a small contribution of methanotrophic archaea and MG-II *Euryarchaeota* (Figure 7). In addition, the good correlation of *Cren* with other individual GDGTs (Supplementary Figure S1a) revealed a similar source of *Thaumarchaeota*. Further, the ratio of *Crenarchaeol* and its regioisomer (*Cren/Cren'*) was 21.8 (Supplementary Table S4), pointing to a mixture of *Thaumarchaeota* group I.1a and 1b [50].

Most brGDGTs were bacteria-derived and potentially sourced from land soil, similar to the case in Weijers Schouten et al., 2009. Under marine environments, particularly fans and deltas, brGDGTs can be derived from mixed marine and land sources. Three indexes, the BIT, the degree of cyclization (DC), and #rings_{tetra}, were applied here to reveal the contribution of brGDGTs.

A small amount of land brGDGTs were revealed by the low BIT (0.02–0.21, Figure 6a), corresponding to the previous study in the Niger fan around 175 km from this study site [51]. The high riverine discharge during the early Holocene was caused by increased precipitation and soil erosion, as the consequence of an intensified WAM [47]. High precipitation led to the high vegetation in the Niger Basin. Furthermore, the DC (average 0.19) revealed the main land brGDGTs during the AHP and a mixture of land and marine autochthonous later (average 0.26, Figure 6a) [32]. The #rings_{tetra} changed greatly in the early Holocene and reached their peak at 5 kyr BP; then, they decreased abruptly. Specifically, they varied from 0.17 to 1.83, indicating the land-derived origin (Supplementary Table S4), which was significantly higher in the marine-derived brGDGTs (>0.7) than the land-derived brGDGTs (<0.7) [13].

The source of OH-GDGTs is complex because of the abundant diversity of archaeal communities. OH-GDGT-2 are abundant in land; the weak correlation between OH-GDGT-2 and brGDGT-1a (Supplementary Figure S1d) indirectly implied that OH-GDGTs were probably dominated by a marine source [52]. The strong correlation (Supplementary Figure S1b) between the OH-GDGTs and isoGDGTs suggested further a common source of marine *Thaumarchaeota*.

5.3. Reconstruction of the SST during the Holocene

The reconstruction of the TEX₈₆-SST may be disturbed by the input of the land isoGDGTs [41] or other in situ marine archaea [30]. As discussed above, the low BIT excluded the influence of land, and the isoGDGTs originated from *Thaumarchaeota* other than marine archaea. Consequently, the TEX₈₆ and RI-OH reconstructed reliable SSTs of the Niger fan.

5.3.1. Modern SSTs

The TEX₈₆-SST (Figure 5) of the top layer was 23.6 °C, 4 °C lower than the current mean annual SST, determined by WOA18 data (<https://www.ncei.noaa.gov/products/world-ocean-atlas>, accessed on 11 October 2022), and close to the summer temperature of 30–40 m subsurface (average 23.8 °C). This layer is the predominant habitation zone of the *Thaumarchaeotal* community in the Guinea Basin [53]. Further, the high surface temperature may cause more ammonia to fertilize *Thaumarchaeota* in the boreal winter in the Guinea Basin, different to other parts of Africa due to the Guinea Current [53,54], TEX^H₈₆ may thus reconstruct a cold bias of the summer subsurface temperature.

The RI-OH-SST (21.3 °C) of the top layer was lower than the TEX₈₆-SST. This low RI-OH SSTs was speculated to represent the annual temperature of the 100–200 m subsurface. The OH-GDGTs, similar to isoGDGTs, might respond differently to shallow- and deep-water communities [55], and the OH-GDGT-based indices correlated with an annual temperature of 100–200 m [33]. However, high river discharge may cause a warm SST rather than the annual mean SSTs, as reported in the Chinese coastal seas [22]. This deviation can be calibrated (Equation (6) in Table 1b); the calibrated top layer temperature was 26.8 °C, close to the modern mean annual SST (27.8 °C). Recently, a strong correlation between the OH-2/OHs and annual SST > 25 °C was reported (Table 1b, Equation (7)) [33]; it is suitable for this area, and the core-top SST was 27.9 °C.

5.3.2. Paleo SSTs

The SSTs reconstructed by the TEX^H₈₆ and RI-OH demonstrated a slight warming since the late Holocene (Figure 5), corresponding to that of the Sanaga River mouth [24].

The GDGTs-SSTs were lower than the Mg/Ca-SST of planktonic foraminifera [24], recovered from a sediment core in the Sanaga River mouth (02°30.0' N, 09°24.3' E, 1328 m water depth). This difference might be caused by the differing season of growth, as *Thaumarchaeota* thrive in the cool “summer”, and planktonic foraminifera flourish during the warm “winter” (Figure 1 Left) [56].

Both the TEX^H₈₆-SST and RI-OH-SST dropped around 2 °C, corresponding to the significant dry spell in the low latitude around 8.4–8.2 kyr BP [46]. Similar short cooling (~2 °C, $\delta^{18}\text{O}$ -SST of *G. bulloides*) has also been reported in the Somalia Basin [44]. A slow cooling of TEX₈₆ and RI-OH SST during the AHP (Figure 5) was due to the weakening monsoon. The eastern equatorial Atlantic SST was mainly controlled by the radiative forcing corresponding to the global monsoon [57]. The coupling of the equatorial Atlantic SST to the WAM resulted in a low SST, weakened atmospheric convection, and reduced monsoonal precipitation. The slow rise of the SSTs after 3 kyr BP, was consistent with the freshwater records in West Africa [47]. This rise was caused by the southward shift of the ITCZ and the strengthened northern trade wind [57].

6. Conclusions

The distribution of GDGTs, $\delta^{13}\text{C}_{\text{org}}$, $\delta^{15}\text{N}$, TOC, and TN in a 2 m sediment core (~8.5 kyr BP) retrieved from the Niger Delta in the GOG was intensively investigated.

All the determined parameters, BIT index, and binary mixing models indicated a mixed OM source of marine and land. The BIT index, MI index, GDGT-2/*Cren*, and *Cren*/*Cren'* revealed the predominant source of GDGT to be the *Thaumarchaeota* group I.1 of archaea. A positive linearity of isoGDGTs and OH-GDGTs suggested that these compounds maybe produced by a common archaeal community. The BIT index, DC, and #rings_{tetra}

supported mainly land inputs of br-GDGT during the early and middle Holocene. Further, the DC revealed a mixture of land and marine autochthonous after the AHP.

Four periods were clearly revealed. In particular, the 8.2 kyr BP event was obviously demonstrated by a low TOC, TN, C/N ratio, BIT index, and a rapid decline in the sedimentation rate. A gradually decrease in land input was indicated by the decreased TOC and C/N after the humid periods (~8 to 5.5 kyr BP).

The millennium-scale SSTs were reconstructed by TEX₈₆ and RI-OH, and they were lower than the Holocene SSTs in the Sanaga River mouth. The habitat depth and growth season of *Thaumarchaeota* possibly caused the low evaluated modern SST. A precise SST was obtained by the calibration of OH-2/OHs. The paleo SSTs dropped slightly during ca. 8.5–8.2 kyr BP, because of the abrupt drought in low-latitude Africa with inconspicuous cooling.

The multiple biomarkers help to shed a light on the source, fate, and dynamics of organic matter and the paleoclimate in the Niger Delta during the Holocene.

Supplementary Materials: The following supporting information can be downloaded at: <https://www.mdpi.com/article/10.3390/w16050771/s1>, Figure S1: Relationship between GDGTs. (a) *Crenarchaeol* and other iso-GDGTs; (b) iso-GDGTs and OH-GDGTs; (c) relationship between TOC and TN; (d) OH-GDGT-2 and br-GDGT-1a; Table S1: Total organic carbon (TOC) and total nitrogen (TN) content, $\delta^{13}\text{C}$ and $\delta^{15}\text{N}$ values, and C/N ratio in core GC10; Table S2: Reconstruction of the paleotemperatures based on TEX₈₆ and RI-OH in core GC10; Table S3: Indices of br-GDGTs and percentage of terrestrial organic carbon based on a binary mixing model of $\delta^{13}\text{C}$ and BIT. Table S4: Various indices were used to evaluate the source of GDGTs; Table S5: Annual average surface seawater temperature (SST) and surface seawater salinity (SSS) data of the equatorial Atlantic from 1955 to 2017 (3.5° N; 5.5° E).

Author Contributions: All authors contributed to the study conception and design. L.L. (Lihua Liu) conceived and supervised the study. L.L. (Lihua Liu), P.Y., S.M., Y.C., M.Z. and L.L. (Li Liu) performed the experiments. P.Y. and Z.Q. analyzed the data. P.Y. and L.L. (Lihua Liu) wrote the manuscript. All authors have read and agreed to the published version of the manuscript.

Funding: This research was funded by the NSF program, grant number [417760711], the Key-Area Research and Development Program of Guangdong Province, grant number [2020B1111010004], Guangdong Special Support Program, grant number [2019BT02L278], and the Major Program of Guangdong Basic and Applied Research, grant number [2019B030302004].

Data Availability Statement: The major contributions presented in the study are included in the Supplementary Materials; further inquiries can be directed to the corresponding author.

Acknowledgments: The authors would like to thank all of the crews and scientists of cruise 57-IV and the critical suggestion from Jianfang Hu from Guangzhou Institute of Geochemistry, Chinese Academy of Sciences.

Conflicts of Interest: The authors declare no conflicts of interest.

References

1. Huguet, C.; Kim, J.H.; Gonzalez-Arango, C.; Ramirez-Valencia, V.; Kang, S.; Gal, J.K.; Shin, K.H. Sources of organic matter in two contrasting tropical coastal environments: The Caribbean Sea and the eastern Pacific. *J. S. Am. Earth Sci.* **2019**, *96*, 102349. [CrossRef]
2. Carneiro, L.M.; Zucchi, M.d.R.; de Jesus, T.B.; Junior, J.B.d.S.; Hadlich, G.M. $\delta^{13}\text{C}$, $\delta^{15}\text{N}$ and TOC/TN as indicators of the origin of organic matter in sediment samples from the estuary of a tropical river. *Mar. Pollut. Bull.* **2021**, *172*, 112857. [CrossRef]
3. Olusegun, D.A.; Qiao, L.; Ding, D.; Li, G.; Ma, Y.; Wang, L. Evolutionary trends of the Niger Delta shoreline during the last 100 years: Responses to rainfall and river discharge. *Mar. Geol.* **2015**, *367*, 202–211.
4. Akinlua, A.; Torto, N. Geochemical evaluation of Niger Delta sedimentary organic rocks: A new insight. *Int. J. Earth Sci.* **2011**, *100*, 1401–1411. [CrossRef]
5. Shanahan, T.M.; McKay, N.P.; Huguen, K.A.; Overpeck, J.T.; Otto-Bliesner, B.; Heil, C.W.; King, J.; Scholz, C.A.; Peck, J. The time-transgressive termination of the African Humid Period. *Nat. Geosci.* **2015**, *8*, 140–144. [CrossRef]
6. Druryan, L.M.; Fulakeza, M. The impact of the Atlantic cold tongue on West African monsoon onset in regional model simulations for 1998–2002. *Int. J. Climatol.* **2015**, *35*, 275–287. [CrossRef]

7. Liao, W.S.; Hu, J.F.; Peng, P.A. Burial of Organic Carbon in the Taiwan Strait. *J. Geophys. Res.-Ocean.* **2018**, *123*, 6639–6652. [\[CrossRef\]](#)
8. Elderfield, H.; Ganssen, G. Past temperature and $\delta^{18}\text{O}$ of surface ocean waters inferred from foraminiferal Mg/Ca ratios. *Nature* **2000**, *405*, 442–445. [\[CrossRef\]](#)
9. Prahl, F.G.; Wakeham, S.G. Calibration of unsaturation patterns in long-chain ketone compositions for paleotemperature assessment. *Nature* **1987**, *330*, 367–369. [\[CrossRef\]](#)
10. Rampen, S.W.; Schouten, S.; Wakeham, S.G.; Damste, J.S.S. Seasonal and spatial variation in the sources and fluxes of long chain diols and mid-chain hydroxy methyl alkanoates in the Arabian Sea. *Org. Geochem.* **2007**, *38*, 165–179. [\[CrossRef\]](#)
11. Yao, P.; Yu, Z.; Bianchi, T.S.; Guo, Z.; Zhao, M.; Knappy, C.S.; Keely, B.J.; Zhao, B.; Zhang, T.; Pan, H.; et al. A multiproxy analysis of sedimentary organic carbon in the Changjiang Estuary and adjacent shelf. *J. Geophys. Res.-Biogeosci.* **2015**, *120*, 1407–1429. [\[CrossRef\]](#)
12. Kim, J.-H.; Crosta, X.; Willmott, V.; Renssen, H.; Bonnin, J.; Helmke, P.; Schouten, S.; Damste, J.S.S. Holocene subsurface temperature variability in the eastern Antarctic continental margin. *Geophys. Res. Lett.* **2012**, *39*. [\[CrossRef\]](#)
13. Schouten, S.; Hopmans, E.C.; Damste, J.S.S. The organic geochemistry of glycerol dialkyl glycerol tetraether lipids: A review. *Org. Geochem.* **2013**, *54*, 19–61. [\[CrossRef\]](#)
14. Hopmans, E.C.; Weijers, J.W.H.; Schefuss, E.; Herfort, L.; Damste, J.S.S.; Schouten, S. A novel proxy for terrestrial organic matter in sediments based on branched and isoprenoid tetraether lipids. *Earth Planet. Sci. Lett.* **2004**, *224*, 107–116. [\[CrossRef\]](#)
15. Damste, J.S.S.; Ossebaard, J.; Schouten, S.; Verschuren, D. Distribution of tetraether lipids in the 25-ka sedimentary record of Lake Challa: Extracting reliable TEX₈₆ and MBT/CBT palaeotemperatures from an equatorial African lake. *Quat. Sci. Rev.* **2012**, *50*, 43–54. [\[CrossRef\]](#)
16. Karner, M.B.; DeLong, E.F.; Karl, D.M. Archaeal dominance in the mesopelagic zone of the Pacific Ocean. *Nature* **2001**, *409*, 507–510. [\[CrossRef\]](#)
17. Liu, X.-L.; Summons, R.E.; Hinrichs, K.-U. Extending the known range of glycerol ether lipids in the environment: Structural assignments based on tandem mass spectral fragmentation patterns. *Rapid Commun. Mass. Spectrom.* **2012**, *26*, 2295–2302. [\[CrossRef\]](#)
18. Peterse, F.; Nicol, G.W.; Schouten, S.; Sinninghe Damsté, J.S. Influence of soil pH on the abundance and distribution of core and intact polar lipid-derived branched GDGTs in soil. *Org. Geochem.* **2010**, *41*, 1171–1175. [\[CrossRef\]](#)
19. Schouten, S.; Hopmans, E.C.; Schefuss, E.; Damste, J.S.S. Distributional variations in marine crenarchaeotal membrane lipids: A new tool for reconstructing ancient sea water temperatures? *Earth Planet. Sci. Lett.* **2002**, *204*, 265–274. [\[CrossRef\]](#)
20. Schouten, S.; Hugué, C.; Hopmans, E.C.; Kienhuis, M.V.M.; Damste, J.S.S. Analytical methodology for TEX₈₆ paleothermometry by high-performance liquid chromatography/atmospheric pressure chemical ionization-mass spectrometry. *Anal. Chem.* **2007**, *79*, 2940–2944. [\[CrossRef\]](#)
21. Kim, J.-H.; van der Meer, J.; Schouten, S.; Helmke, P.; Willmott, V.; Sangiorgi, F.; Koç, N.; Hopmans, E.C.; Damsté, J.S.S. New indices and calibrations derived from the distribution of crenarchaeal isoprenoid tetraether lipids: Implications for past sea surface temperature reconstructions. *Geochim. Cosmochim. Acta* **2010**, *74*, 4639–4654. [\[CrossRef\]](#)
22. Lü, X.; Liu, X.-L.; Elling, F.J.; Yang, H.; Xie, S.; Song, J.; Li, X.; Yuan, H.; Li, N.; Hinrichs, K.-U. Hydroxylated isoprenoid GDGTs in Chinese coastal seas and their potential as a paleotemperature proxy for mid-to-low latitude marginal seas. *Org. Geochem.* **2015**, *89–90*, 31–43. [\[CrossRef\]](#)
23. Umoh, U.U.; Li, L.; Wang, J.; Kauluma, N.; Asuquo, F.E.; Akpan, E.R. Glycerol dialkyl glycerol tetraether signatures in tropical mesotidal estuary sediments of Qua Iboe River, Gulf of Guinea. *Org. Geochem.* **2022**, *170*, 104461. [\[CrossRef\]](#)
24. Weldeab, S.; Lea, D.W.; Schneider, R.R.; Andersen, N. 155,000 years of West African monsoon and ocean thermal evolution. *Science* **2007**, *316*, 1303–1307. [\[CrossRef\]](#)
25. Corredor, F.; Shaw, J.H.; Bilotti, F.; Tuttle, M.L.W.; Charpentier, R.R.; Brownfield, M.E. Structural styles in the deep-water fold and thrust belts of the Niger Delta (June, pg 753, 2005). *Aapg Bull.* **2013**, *97*, 2102.
26. Atkinson, B.W. Atmosphere, Weather And Climate, 6th Edition—Barry, Rg, Chorley, R.J. *Appl. Geogr.* **1993**, *13*, 373. [\[CrossRef\]](#)
27. Marret, F. Distribution of dinoflagellate cysts in recent marine-sediments from the east equatorial atlantic (gulf of guinea). *Rev. Palaeobot. Palynol.* **1994**, *84*, 1–22. [\[CrossRef\]](#)
28. Dada, O.A.; Li, G.; Qiao, L.; Ding, D.; Ma, Y.; Xu, J. Seasonal shoreline behaviours along the arcuate Niger Delta coast: Complex interaction between fluvial and marine processes. *Cont. Shelf Res.* **2016**, *122*, 51–67. [\[CrossRef\]](#)
29. Heaton, T.J.; Koehler, P.; Butzin, M.; Bard, E.; Reimer, R.W.; Austin, W.E.N.; Ramsey, C.B.; Grootes, P.M.; Hughen, K.A.; Kromer, B.; et al. MARINE20—The marine radiocarbon age calibration curve (0–55,000 CAL BP). *Radiocarbon* **2020**, *62*, 779–820. [\[CrossRef\]](#)
30. Zhang, Y.G.; Zhang, C.L.; Liu, X.-L.; Li, L.; Hinrichs, K.-U.; Noakes, J.E. Methane Index: A tetraether archaeal lipid biomarker indicator for detecting the instability of marine gas hydrates. *Earth Planet. Sci. Lett.* **2011**, *307*, 525–534. [\[CrossRef\]](#)
31. Sinninghe Damsté Jaap, S.; Rijpstra, W.I.C.; Hopmans Ellen, C.; Jung, M.-Y.; Kim, J.-G.; Rhee, S.-K.; Stieglmeier, M.; Schleper, C. Intact Polar and Core Glycerol Dibiphytanyl Glycerol Tetraether Lipids of Group I.1a and I.1b Thaumarchaeota in Soil. *Appl. Environ. Microbiol.* **2012**, *78*, 6866–6874. [\[CrossRef\]](#)
32. Damste, J.S.S.; Ossebaard, J.; Abbas, B.; Schouten, S.; Verschuren, D. Fluxes and distribution of tetraether lipids in an equatorial African lake: Constraints on the application of the TEX₈₆ palaeothermometer and BIT index in lacustrine settings. *Geochim. Cosmochim. Acta* **2009**, *73*, 4232–4249. [\[CrossRef\]](#)

33. Yang, Y.; Gao, C.; Dang, X.; Ruan, X.; Lu, X.; Xie, S.; Li, X.; Yao, Y.; Yang, H. Assessing hydroxylated isoprenoid GDGTs as a paleothermometer for the tropical South China Sea. *Org. Geochem.* **2018**, *115*, 156–165. [\[CrossRef\]](#)
34. Emerson, S.; Hedges, J.I. Processes controlling the organic carbon content of open ocean sediments. *Paleoceanography* **1988**, *3*, 621–634. [\[CrossRef\]](#)
35. Meyers, P.A. Organic geochemical proxies of paleoceanographic, paleolimnologic, and paleoclimatic processes. *Org. Geochem.* **1997**, *27*, 213–250. [\[CrossRef\]](#)
36. Schoeninger, M.J.; Deniro, M.J. Nitrogen and carbon isotopic composition of bone-collagen from marine and terrestrial animals. *Geochim. Cosmochim. Acta* **1984**, *48*, 625–639. [\[CrossRef\]](#)
37. Liu, M.; Hou, L.J.; Xu, S.Y.; Ou, D.N.; Yang, Y.; Yu, J.; Wang, Q. Organic carbon and nitrogen stable isotopes in the intertidal sediments from the Yangtze Estuary, China. *Mar. Pollut. Bull.* **2006**, *52*, 1625–1633. [\[CrossRef\]](#)
38. Goni, M.A.; Ruttenberg, K.C.; Eglinton, T.I. A reassessment of the sources and importance of land-derived organic matter in surface sediments from the Gulf of Mexico. *Geochim. Cosmochim. Acta* **1998**, *62*, 3055–3075. [\[CrossRef\]](#)
39. Herfort, L.; Schouten, S.; Boon, J.P.; Damste, J.S.S. Application of the TEX₈₆ temperature proxy to the southern North Sea. *Org. Geochem.* **2006**, *37*, 1715–1726. [\[CrossRef\]](#)
40. Sobrinho, R.d.L.; Bernardes, M.C.; de Rezende, C.E.; Kim, J.-H.; Schouten, S.; Damste, J.S.S. A multiproxy approach to characterize the sedimentation of organic carbon in the Amazon continental shelf. *Mar. Chem.* **2021**, *232*, 103961. [\[CrossRef\]](#)
41. Weijers, J.W.H.; Schouten, S.; Spaargaren, O.C.; Sinninghe Damsté, J.S. Occurrence and distribution of tetraether membrane lipids in soils: Implications for the use of the TEX₈₆ proxy and the BIT index. *Org. Geochem.* **2006**, *37*, 1680–1693. [\[CrossRef\]](#)
42. Collins, J.A.; Schefuss, E.; Heslop, D.; Mulitza, S.; Prange, M.; Zabel, M.; Tjallingii, R.; Dokken, T.M.; Huang, E.; Mackensen, A.; et al. Interhemispheric symmetry of the tropical African rainbelt over the past 23,000 years. *Nat. Geosci.* **2011**, *4*, 42–45. [\[CrossRef\]](#)
43. Weldeab, S.; Lea, D.W.; Schneider, R.R.; Andersen, N. Centennial scale climate instabilities in a wet early Holocene West African monsoon. *Geophys. Res. Lett.* **2007**, *34*. [\[CrossRef\]](#)
44. Alley, R.B.; Agustsdottir, A.M. The 8k event: Cause and consequences of a major Holocene abrupt climate change. *Quat. Sci. Rev.* **2005**, *24*, 1123–1149. [\[CrossRef\]](#)
45. Kendall, R.A.; Mitrovica, J.X.; Milne, G.A.; Tornqvist, T.E.; Li, Y. The sea-level fingerprint of the 8.2 ka climate event. *Geology* **2008**, *36*, 423–426. [\[CrossRef\]](#)
46. Gasse, F. Hydrological changes in the African tropics since the Last Glacial Maximum. *Quat. Sci. Rev.* **2000**, *19*, 189–211. [\[CrossRef\]](#)
47. Cole, J.M.; Goldstein, S.L.; Demenocal, P.B.; Hemming, S.R.; Grousset, F.E. Contrasting compositions of Saharan dust in the eastern Atlantic Ocean during the last deglaciation and African Humid Period. *Earth Planet. Sci. Lett.* **2009**, *278*, 257–266. [\[CrossRef\]](#)
48. Blaga, C.I.; Reichart, G.-J.; Heiri, O.; Damste, J.S.S. Tetraether membrane lipid distributions in water-column particulate matter and sediments: A study of 47 European lakes along a north-south transect. *J. Paleolimnol.* **2009**, *41*, 523–540. [\[CrossRef\]](#)
49. Weijers, J.W.H.; Lim, K.L.H.; Aquilina, A.; Damste, J.S.S.; Pancost, R.D. Biogeochemical controls on glycerol dialkyl glycerol tetraether lipid distributions in sediments characterized by diffusive methane flux. *Geochem. Geophys. Geosyst.* **2011**, *12*. [\[CrossRef\]](#)
50. Li, J.; Pancost, R.D.; Naafs, B.D.A.; Yang, H.; Zhao, C.; Xie, S. Distribution of glycerol dialkyl glycerol tetraether (GDGT) lipids in a hypersaline lake system. *Org. Geochem.* **2016**, *99*, 113–124. [\[CrossRef\]](#)
51. Kallweit, W.; Mollenhauer, G.; Zabel, M. Multi-proxy reconstruction of terrigenous input and sea-surface temperatures in the eastern Gulf of Guinea over the last similar to 35 ka. *Mar. Geol.* **2012**, *319*, 35–46. [\[CrossRef\]](#)
52. Kang, S.; Shin, K.-H.; Kim, J.-H. Occurrence and distribution of hydroxylated isoprenoid glycerol dialkyl glycerol tetraethers (OH-GDGTs) in the Han River system, South Korea. *Acta Geochim.* **2017**, *36*, 367–369. [\[CrossRef\]](#)
53. Park, E.; Hefter, J.; Fischer, G.; Mollenhauer, G. TEX₈₆ in sinking particles in three eastern Atlantic upwelling regimes. *Org. Geochem.* **2018**, *124*, 151–163. [\[CrossRef\]](#)
54. Pitcher, A.; Wuchter, C.; Siedenberg, K.; Schouten, S.; Damste, J.S.S. Crenarchaeol tracks winter blooms of ammonia-oxidizing Thaumarchaeota in the coastal North Sea. *Limnol. Oceanogr.* **2011**, *56*, 2308–2318. [\[CrossRef\]](#)
55. Wei, B.; Jia, G.; Hefter, J.; Kang, M.; Park, E.; Wang, S.; Mollenhauer, G. Comparison of the U-37(K'), LDI, TEX₈₆^H, and RI-OH temperature proxies in sediments from the northern shelf of the South China Sea. *Biogeosciences* **2020**, *17*, 4489–4508. [\[CrossRef\]](#)
56. Timmermann, A.; Sachs, J.; Timm, O.E. Assessing divergent SST behavior during the last 21 ka derived from alkenones and G. ruber-Mg/Ca in the equatorial Pacific. *Paleoceanography* **2014**, *29*, 680–696. [\[CrossRef\]](#)
57. Weldeab, S.; Schneider, R.R.; Kolling, M.; Wefer, G. Holocene African droughts relate to eastern equatorial Atlantic cooling. *Geology* **2005**, *33*, 981–984. [\[CrossRef\]](#)

Disclaimer/Publisher's Note: The statements, opinions and data contained in all publications are solely those of the individual author(s) and contributor(s) and not of MDPI and/or the editor(s). MDPI and/or the editor(s) disclaim responsibility for any injury to people or property resulting from any ideas, methods, instructions or products referred to in the content.